Does Long-Term GPS in the Western Alps Finally Confirm Earthquake Mechanisms?

A. Walpersdorf, L. Pinget, P. Vernant, C. Sue, A. Deprez, Stéphane Baize, Pascale Bascou, Sandrine Baudin, Olivier Bock, Pierre Briole, et al.

▶ **To cite this version:**

A. Walpersdorf, L. Pinget, P. Vernant, C. Sue, A. Deprez, et al.. Does Long-Term GPS in the Western Alps Finally Confirm Earthquake Mechanisms?. Tectonics, 2018, 37 (10), pp.3721-3737. 10.1029/2018TC005054 . hal-01947724

HAL Id: hal-01947724
https://hal.science/hal-01947724

Submitted on 20 Feb 2019

HAL is a multi-disciplinary open access archive for the deposit and dissemination of scientific research documents, whether they are published or not. The documents may come from teaching and research institutions in France or abroad, or from public or private research centers.

L'archive ouverte pluridisciplinaire **HAL**, est destinée au dépôt et à la diffusion de documents scientifiques de niveau recherche, publiés ou non, émanant des établissements d'enseignement et de recherche français ou étrangers, des laboratoires publics ou privés.

Tectonics

RESEARCH ARTICLE
10.1029/2018TC005054

Special Section:
Geodynamics, Crustal and Lithospheric Tectonics, and active deformation in the Mediterranean Regions (A tribute to Prof. Renato Funiciello)

Does Long-Term GPS in the Western Alps Finally Confirm Earthquake Mechanisms?

A. Walpersdorf[1], L. Pinget[1], P. Vernant[2], C. Sue[3], A. Deprez[1], and the RENAG team

[1]University Grenoble Alpes, University Savoie Mont Blanc, CNRS, IRD, IFSTTAR, ISTerre, Grenoble, France, [2]Geosciences Montpellier, University of Montpellier, CNRS, Montpellier, France, [3]Chrono-Environnement Besançon, OSU THETA, University Bourgogne-Franche-Comté, Besançon, France

Abstract The availability of GPS survey data spanning 22 years, along with several independent velocity solutions including up to 16 years of permanent GPS data, presents a unique opportunity to search for persistent (and thus reliable) deformation patterns in the Western Alps, which in turn allow a reinterpretation of the active tectonics of this region. While GPS velocities are still too uncertain to be interpreted on an individual basis, the analysis of range-perpendicular GPS velocity profiles clearly highlights zones of extension in the center of the belt (15.3 to 3.1 nanostrain/year from north to south), with shortening in the forelands. The contrasting geodetic deformation pattern is coherent with earthquake focal mechanisms and related strain/stress patterns over the entire Western Alps. The GPS results finally provide a reliable and robust quantification of the regional strain rates. The observed vertical motions of 2.0 to 0.5 mm/year of uplift from north to south in the core of the Western Alps is interpreted to result from buoyancy forces related to postglacial rebound, erosional unloading, and/or viscosity anomalies in the crustal and lithospheric root. Spatial decorrelation between vertical and horizontal (seismicity related) deformation calls for a combination of processes to explain the complex present-day dynamics of the Western Alps.

RENAG team members are listed in the Appendix.

Key Points:
- Twenty-two years of survey and 16 years of permanent GPS data analyzed in several independent solutions highlight persistent deformation patterns in the Western Alps
- GPS data show extension in the center of the belt and compression along the eastern and western forelands, coherent with earthquake focal mechanisms
- Spatial decorrelation between uplift and co-located extension and seismicity calls for a complex process driving the present-day dynamics of the Western Alps

Correspondence to:
A. Walpersdorf,
andrea.walpersdorf@univ-grenoble-alpes.fr

Citation:
Walpersdorf, A., Pinget, L., Vernant, P., Sue, C., Deprez, A., & the RENAG team (2018). Does long-term GPS in the Western Alps finally confirm earthquake mechanisms? *Tectonics*, *37*, 3721–3737. https://doi.org/10.1029/2018TC005054

Received 13 MAR 2018
Accepted 28 AUG 2018
Accepted article online 3 SEP 2018
Published online 18 OCT 2018

©2018. The Authors.
This is an open access article under the terms of the Creative Commons Attribution-NonCommercial-NoDerivs License, which permits use and distribution in any medium, provided the original work is properly cited, the use is non-commercial and no modifications or adaptations are made.

1. Introduction

The Western Alps form the highest topography in Europe (more than 80 summits above 4,000 m), and feature the highest present-day uplift rates in Western Europe (Serpelloni et al., 2013). However, the convergence between Nubia and Eurasia at a rate of ~5 mm/year (e.g., Nocquet & Calais, 2004; Nocquet et al., 2006) cannot explain this uplift as the Corso-Sardinia block shows no significant motion with respect to stable Europe (Nocquet, 2012), indicating that the major plate boundary is situated along the Maghreb region of Northern Africa. This is reflected in seismicity (Figure 1), which runs along the North African coast (west of 10°E), spreading north to engulf the Adriatic and Apulian microplates (east of 10°E) before reaching Greece. The western limit of the Adriatic microplate runs through the Western Alps. The microplate is further delimited to the north by the central Alps and the Dinarides, and to the south by the Apennines. The Adriatic plate is rotating counterclockwise around a pole that is not precisely determined and probably situated in the north of the Pô plain (Anderson & Jackson, 1987; Calais et al., 2002; Serpelloni et al., 2007). This first order block model explains extension in the Apennines and shortening in the Eastern Alps and the Dinarides, but has several limitations. One of them concerns the motions north of the Apennines along the Italian peninsula, which cannot be explained by a single block, instead requiring a second microblock comprising Apulia in southern Italy (Battaglia et al., 2004; Calais et al., 2002; D'Agostino et al., 2008). Other limitations arise from (1) the rotation pole close to the Western Alps, which is hard to determine due to the very low velocities expected close to the pole, and (2) any departures from the rigid block hypothesis of the Pô plain region.

Numerous works have addressed the kinematics and geodynamics of the Western Alps (see section 2), which indicate that the major deformation style of the Western Alps is dominated at the present day by uplift, most likely induced by body forces rather than rigid plate interactions (i.e., plate tectonics). Nevertheless, moderate but persisting seismicity in this region indicates extensional and transtensional deformation (Figure 1). Here we use two decades of continuous and survey GPS measurements, processed in several independent geodetic solutions to obtain a detailed geodetic 3-D deformation pattern for the Western Alps, which is then compared with the seismic activity. To do so, we carefully evaluate the precision of the survey and permanent GPS measurements, thus enabling the determination of slow deformation patterns of the order of 0.2 mm/year. Furthermore, we take advantage of the redundancy between nearby or independent station velocity estimates to increase the weak signal-to-noise level. Finally, we discuss the resulting deformation signals.

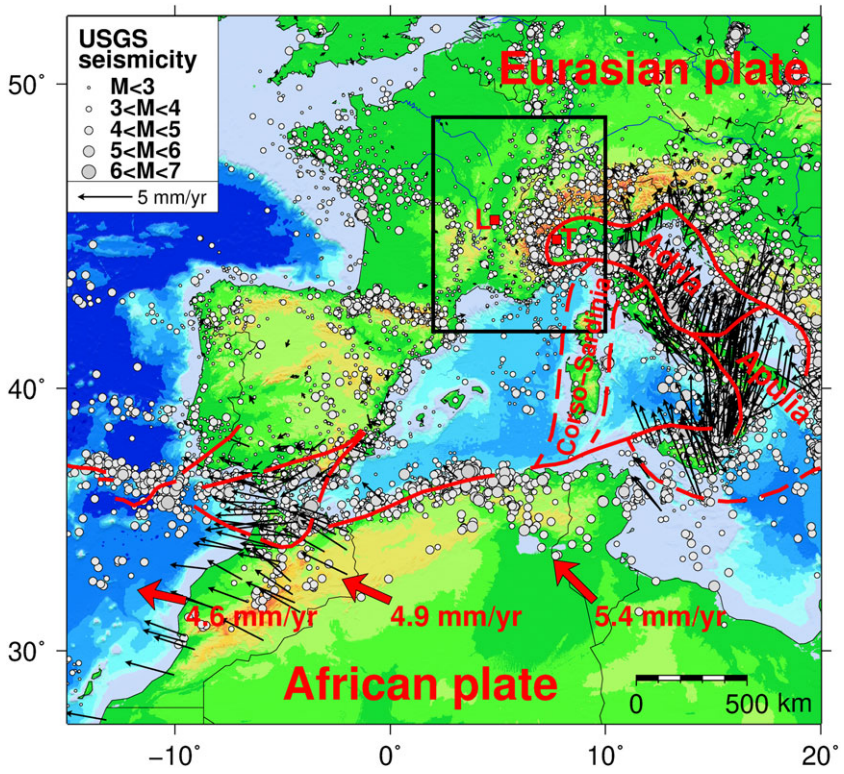

Figure 1. Seismotectonic context of the study region marked by the black rectangle. Gray dots indicate USGS seismicity with magnitudes $>M$ = 2.5 from 2000 to 2017 (https://earthquake.usgs.gov/). African plate velocities with respect to Eurasia (red vectors) are from Serpelloni et al. (2007). The Eurasia-Africa plate boundary and the limits of the Adriatic, Apulian, and Corso-Sardinian block shown by the red lines, as well as the black GPS velocity vectors are from Nocquet (2012). The red squares marked L and T indicate the location of Lyon and Torino, respectively.

2. Previous Works

The key feature providing the boundary conditions for the Western Alpine present-day deformation is the relative motion of the Adriatic plate with respect to stable Europe. Based on different data sets, three different rotation poles have been presented by Calais et al. (2002), Serpelloni et al. (2005), and D'Agostino et al. (2008). While all poles predict small velocities in the Western Alps, they imply different kinematic boundary conditions across a line connecting Lyon and Turin (Torino), in the rigid block context. The pole of Calais et al. (2002), situated close to Milan (9.10°E, 45.36°N), implies 1.3 mm/year of right-lateral strike slip, the pole of Serpelloni et al. (2005) (6.53°E, 44.07°N) suggests 0.5 mm/year of shortening, while the pole of D'Agostino et al. (2008) (7.78°E, 45.79°N) yields 0.6 mm/year of extension. The analysis of more recent available GPS data (Nocquet, 2011) yields rigid block rotations resulting in 0.15 mm/year of extension to 0.42 mm/year of right-lateral strike slip accommodated across the Western Alps. The review of GPS measurements around the Mediterranean Sea by Nocquet (2011) indicates simply an upper limit of 1 mm/year of deformation across the Western Alps. Vigny et al. (2002) estimated the deformation in the inner part of the Western Alpine belt through the analysis of a network of 52 survey sites encompassing mainly the French part of the Alps, but including some stations in Italy and Switzerland, measured between 1993 and 1998. Combining the full velocity field into a single strain rate tensor, the authors found pure extension perpendicular to the belt of 3.2 nanostrain/year oriented 116°N. A component of extension within the range is also proposed by Calais et al. (2002), based on processing of the first permanent GPS data in the Western Alps. The concentration of earthquakes with EW oriented extensional focal mechanisms in the southwestern Alps (suggesting a possible accumulation of present-day deformation in this zone) motivated the geodetic study of Sue et al. (2000). Remeasurement of the dense local campaign network by Walpersdorf et al. (2015) showed EW extension (16 nanostrain/year or 0.5 mm/year across the 30-km-wide network) over a measurement interval of

15 years. Thanks to the long observation span, the GPS velocities converged, reaching values below 1 mm/year, indicating geodetic deformation of the same style and amplitude as the seismic deformation recorded over 37 years (Sue, Delacou, Champagnac, Allanic, Burkhard, 2007). A pattern of extension in the inner belt (along the Penninic front), combined with localized zones of compression along the foothills of the range, has been proposed from the analysis of focal mechanisms (Delacou et al., 2004; Sue et al., 1999). This suggested that gravity collapse could play a role in the present-day deformation of the Western Alps, besides the abovementioned plate tectonic mechanisms. However, Nocquet (2011), Serpelloni et al. (2013), Nocquet et al. (2016), and Nguyen et al. (2016) showed that present-day uplift of 2+ mm/year is occurring in the northern part of the Western Alps. This prohibits deformation mechanisms such as tectonic extension or gravitational collapse as a unique driving force, as they are both related to regional subsidence. Possible driving forces explaining an uplift one magnitude larger than the horizontal deformation and in particular the simultaneous presence of extension and uplift have been discussed by Gardi et al. (2010), Vernant et al. (2013), Nocquet et al. (2016), and Chéry et al. (2016). Through viscoelastic modeling, Gardi et al. (2010) explore whether different driving forces can explain the present-day deformation, concluding buoyancy forces to be important. Vernant et al. (2013) present a model incorporating erosional unloading to explain simultaneous uplift and extension in the core of a mountain belt, as well as compression in the forelands. Nocquet et al. (2016) show that neither the cumulative effect of postglacial rebound at different spatiotemporal scales nor erosional unloading (see also Barletta et al., 2006; Champagnac et al., 2007; Stocchi et al., 2005) can explain the total amount of observed uplift. The region of residual uplift is situated above a zone of relatively low viscosity in the mantle (Lippitsch, 2003; Zhao et al., 2015), where more buoyant mantle material could sustain the Alpine topography in a dynamic way. Finally, Chéry et al. (2016) were able to model a localized zone of uplift in the northwestern Alps by considering postglacial rebound following the Last Glacial Maximum, combined with a laterally variable rheology of the lower crust and the upper mantle beneath the Western Alps. For the Eastern Alps, Mey et al. (2016) also used variations in lithospheric rigidity and rebound due to the Last Glacial Maximum to explain the uplift rates.

3. Data, Analysis Strategy, and Validations

We used the data from (1) the permanent RENAG network (RESIF, 2017; http://renag.resif.fr, in blue on Figure 2) with the first stations beginning operation in 1998 and from (2) the French Reference network RGP (http://rgp.ign.fr) run by the National Geographic Institute, IGN (in white on Figure 2), with stations operating essentially since 2007. Both networks contribute to the French Seismic and geodetic network RESIF (http://www.resif.fr; sponsored by the French National Institute of Earth and Planetary Sciences INSU). While the RENAG network aims at providing continuous GPS (cGPS) data for Earth Science applications with long-term operation of stations installed on stable monuments, the RGP network of IGN is a public service providing access to the French reference system RGF93, and is composed mainly of stations maintained by private societies and public institutions like cities and schools. Five Italian stations are from the cGPS network of the Interreg-B project ALPS-GPSQUAKENET, and one is from the RING network of INGV (http://ring.gm.ingv.it).

The cGPS network in the French Alps can be densified by the GPS Alps survey network (sGPS), which includes 52 sites in France, Switzerland, and Italy, and was established in 1993 and later surveyed in 1998, 2004, and 2015 (black and red squares on Figure 2). The black squares show the sites that have been surveyed up until 2004, while the red ones have also been remeasured in 2015. The results obtained for the first two surveys are available in Vigny et al. (2002).

We quantify the resolution and precision of the GPS measurements, first by comparing sGPS- and cGPS-derived velocity fields and then by comparing different independent geodetic solutions for the same cGPS sites. Once the precision of the station velocities is established, we analyze the obtained velocity fields using different methods discussed in section 3.

After studying maximum permissible deformation rates in the New Madrid seismic zone, Calais and Stein (2009) suggested a decrease in the GPS velocity values with increasing observation span. We present the velocity field of the Alps campaign network after measurement spans of 5, 11, and 22 years in green, red, and black, respectively (Figure 3). For most stations, the velocity decreases in amplitude with increasing

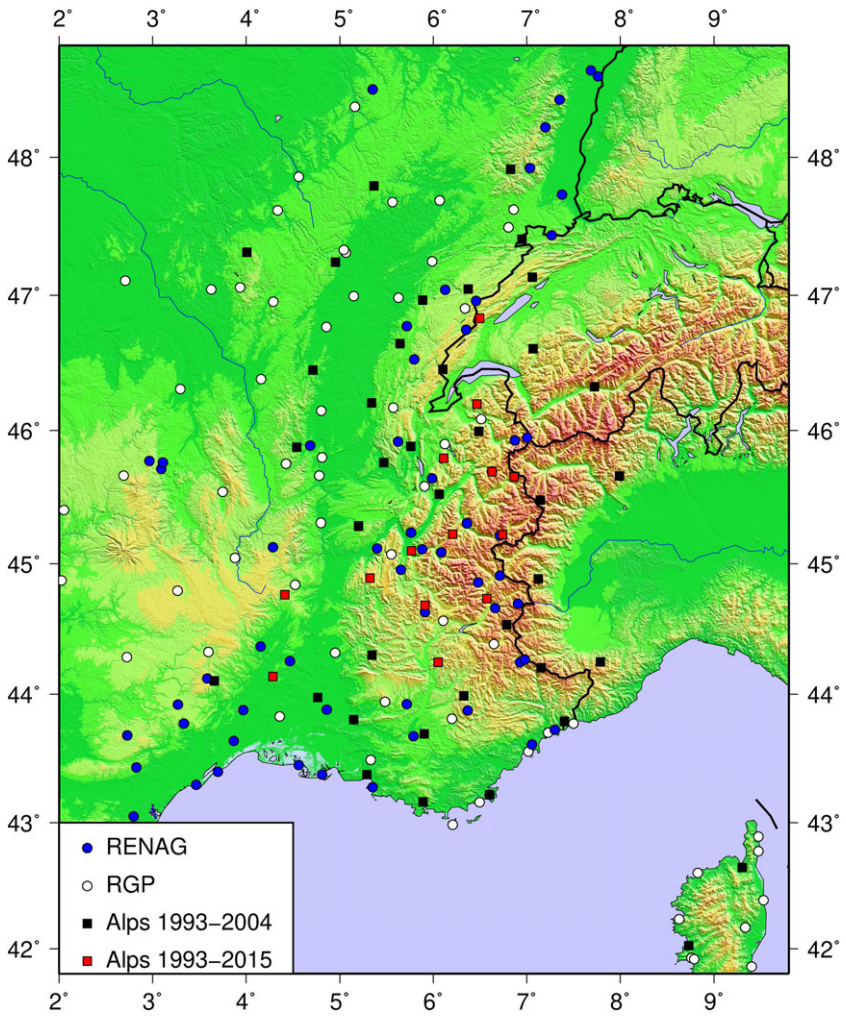

Figure 2. GPS network configurations of the RENAG (blue dots; http://renag.resif.fr), the RGP (white dots; http://rgp.ign.fr), and the Alps campaign (black and red squares for stations measured until 2004 and 2015, respectively; http://gpscope.dt.insu.cnrs.fr).

measurement duration; the velocities of the 14 stations remeasured in 2015 have the longest time span and are very small. The average amplitudes decrease from 1.21 mm/year after 5 years of measurement to 0.98 mm/year after 11 years, finally reaching 0.37 mm/year after 22 years. From long-term cGPS measurements, we expect a tectonic signal with velocity amplitudes of about 0.2 mm/year in the Western Alps. According to two alternative end-member models (a linear decrease as suggested by our 3 data points, and a more realistic logarithmic decrease taking into account the color noise content of GPS time series), we would reach these 0.2 mm/year in 2018 if the amplitudes decrease linearly, but if the decrease is logarithmic, significant velocity amplitudes would be obtained after a measurement span of 35 years in 2028.

The velocity field of the 52 campaign sites in its present state (Figure 3) is still noisy because it includes the stations with only 11 years of observations. However, we can compare the sites with 22 years of measurement with nearby permanent stations (both the campaign and the permanent velocity fields are shown in Figure 4). Twelve of these 14 campaign sites are situated close to permanent sites (within 16 km on average; couples highlighted by yellow rectangles in Figure 4). These 12 couples show average velocity differences of 0.16, 0.22, and 1.65 mm/year on the N, E, and U components, respectively. This strong coherency is encouraging to maintain GPS campaigns over decadal time spans.

As a consequence of this good correlation between long-term campaign observations and permanent measurements, Figure 4 and Table 1 present the final ISTerre solution with a velocity field based on the

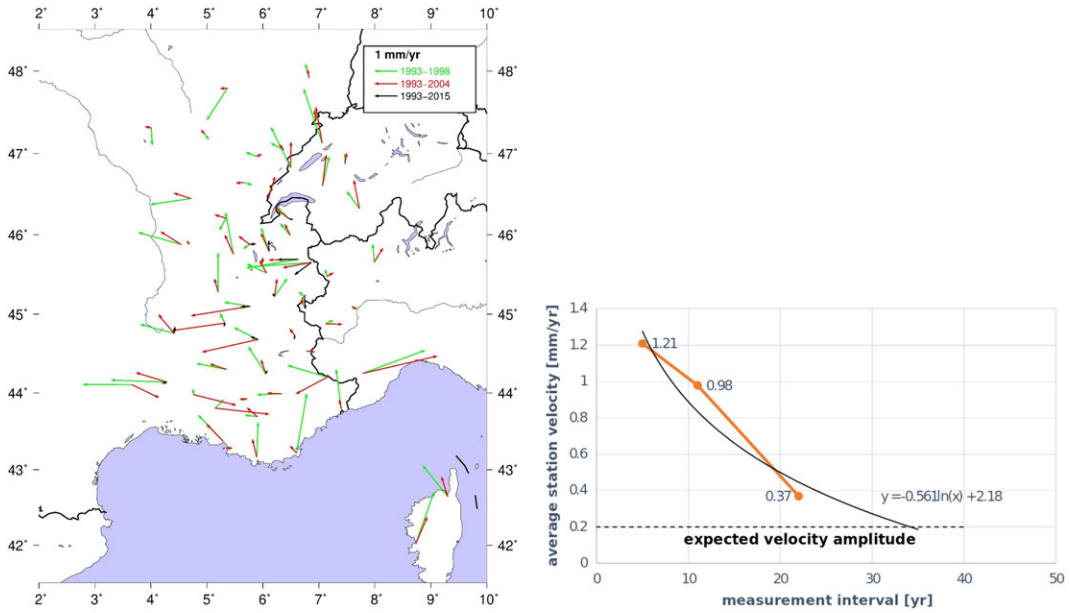

Figure 3. (left) sGPS Alps velocity fields after 5, 11, and 22 years of measurement interval with respect to stable Eurasia, indicated by red, green, and black vectors, respectively. (right) Average velocity amplitudes versus time. A logarithmic fit to the three data points is indicated by the black curve. The horizontal dashed line indicates the level of the expected tectonic signal in the Western Alps.

RENAG network with data from 1998 to mid-2014 (black vectors), and including the Alps campaign sites measured over 22 years (red vectors).

The data analysis of the ISTerre solution was done in a double-differenced strategy with the GAMIT/GLOBK 10.6 software (Herring et al., 2015). Two other independent geodetic solutions were available for this work: (1) from Géosciences Montpellier (called LGM hereafter) made with the Canadian software CSRS-PPP in PPP strategy (Héroux & Kouba, 2001), which includes data from RENAG and RGP from 2000 to 2013, and (2) from the Nevada Geodetic Laboratory (called NGL hereafter), running a solution with GIPSY/OASIS in PPP strategy (Zumberge et al., 1997) from 1998 to 2016.5, combining thousands of permanent GPS stations with freely available data, from which we extracted only the RENAG stations (http://geodesy.unr.edu/NGLStationPages/GlobalStationList). In the following, these independent solutions are compared to establish the degree of coherency in a context of a very slow deformation.

Figure 5 presents the superposition of the ISTerre and LGM solutions after minimizing the differences of site velocities of common stations in both solutions using the VELROT routine of the GAMIT/GLOBK package based on translation and rotation of the solution to be compared. At the level of the slow deformation occurring within France, significant differences persist at certain sites that can be rapidly identified as the youngest stations of the network, yielding different velocity estimates due to the different analysis strategies. On average, the velocity differences can be quantified at 0.13 mm/year (horizontal component) and 0.44 mm/year (vertical component) using 53+ sites common to the two solutions. The same superposition has been done with the ISTerre and the NGL solution yielding average differences over 55 common sites of 0.18 and 0.75 mm/year for the horizontal and the vertical components, respectively. The slightly degraded comparison on the vertical component is probably related to the purely automatic postprocessing of the GPS time series in the NGL solution, missing some offsets which are not documented by equipment changes in the station log sheets.

In summary, our comparisons indicate a level of coherence of long-term sGPS sites with respect to cGPS sites of 0.2 mm/year on the horizontal component. The independent solutions of permanent networks show a similar level of 0.2 mm/year of coherence between each other. Nevertheless, 0.2 mm/year is probably the amplitude of the signal in this low deformation context. Therefore, we chose not to interpret individual station velocities, but to search for redundancy between nearby stations or between independent solutions to increase the signal to noise level.

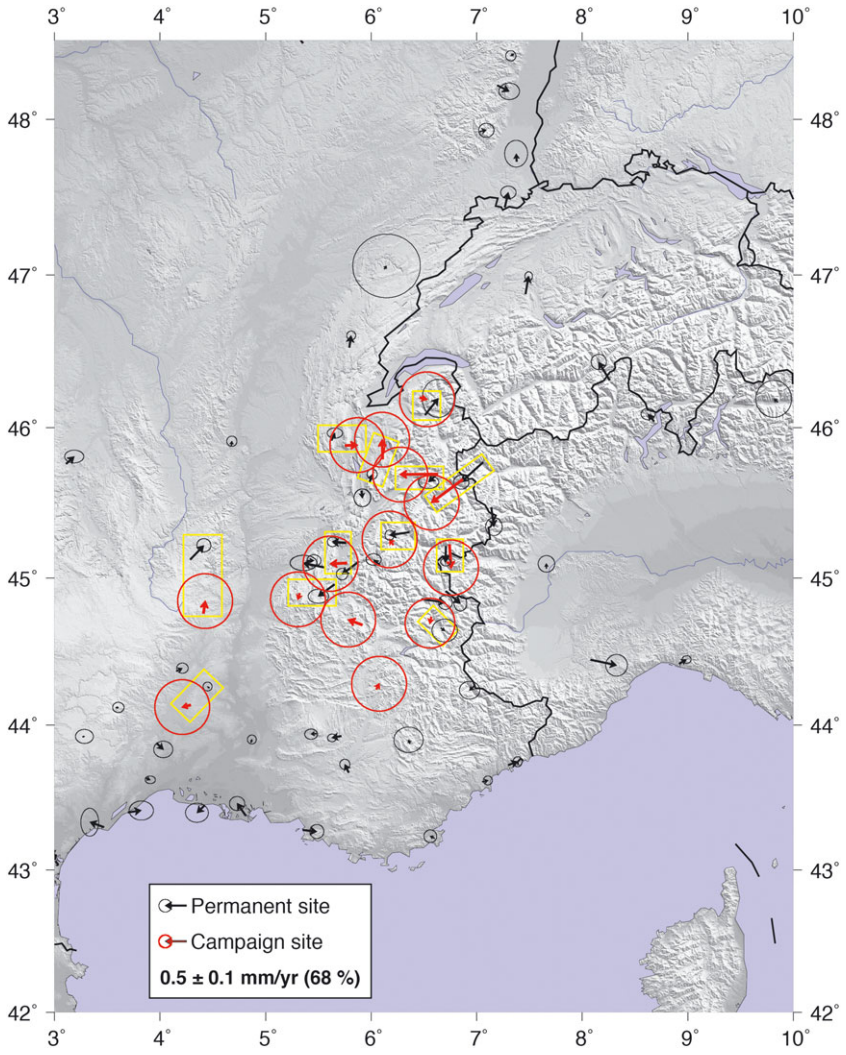

Figure 4. ISTerre final velocity solution with respect to stable Eurasia combining cGPS stations of the RENAG network (black vectors) with sGPS sites measured over 22 years (red vectors). Twelve couples of nearby permanent and campaign stations are highlighted by yellow rectangles.

4. Using Redundancy of the Velocity Fields to Decipher the Deformation Pattern of the Western Alps

4.1. Single Strain Rate Tensor Over the Western Alps

We started by computing a single strain rate tensor with the ISTerre solution for the whole Western Alpine arc. We have chosen two network geometries, one encompassing the sites in the Western Alps and beyond the forelands and one restricted to the stations inside the Alpine belt (Figure 6, black and red symbols, respectively, numerical values in Table 2). The resulting strain rate tensors have a similar aspect, showing mainly east-west extension. The main difference occurs in the strain rate amplitude, 0.67 nanostrain/year (or a velocity difference of 0.067 mm/year over 100-km distance; black tensor) for the large network, and 3.23 nanostrain/year (or 0.323 mm/year over 100 km; red tensor) in the narrow network. The width of the large network is twice the width of the narrow one; hence, the difference in strain rate indicates that the zone of extensional deformation is limited to the Alpine belt and that the Alpine foreland is stable or experiencing shortening. The strain rate tensors computed with or without the sGPS data are consistent. This similarity shows that the sGPS velocity field is coherent with the cGPS one. As a reminder, the preliminary strain rate evaluation by Vigny et al. (2002) yielded 3.5 nanostrain/year over the large network extent, which is consistent with a decrease of GPS velocity amplitudes by a factor of 5 since the 1998 measurement.

Table 1
ISTerre Velocities in the Western Alps With Respect to Stable Eurasia

Longitude (°E)	Latitude (°N)	V_{east} (mm/year)	V_{north} (mm/year)	Sig V_{east} (mm/year)	Sig V_{north} (mm/year)	Corr.	V_{vert} (mm/year)	Sig V_{vert} (mm/year)	Corr.	SITE	Network
3.11108	45.76096	0.19	0.17	0.15	0.10	−0.003	−0.05	−0.53	0.44	CLFD	
3.26826	43.91981	0.04	0.01	0.14	0.11	−0.002	−0.02	−0.25	0.42	SLVT	
3.46643	43.29638	−0.33	0.12	0.14	0.22	−0.000	−0.12	−0.13	0.46	AGDE	
3.58126	44.12140	0.06	0.00	0.09	0.08	−0.003	0.07	0.07	0.36	AIGL	
3.65744	44.10395	1.60	−0.64	0.63	0.63	0.001	2.50	2.50	1.03	CPA0	S04
3.69912	43.39765	0.31	0.05	0.19	0.15	0.000	−0.52	−0.13	0.43	SETE	
3.86412	43.63876	0.11	−0.05	0.08	0.06	−0.006	−0.83	−0.64	0.25	MTP2	
3.96697	43.87690	0.16	−0.15	0.15	0.13	0.000	0.18	−0.27	0.66	BAUB	
4.00745	47.31416	0.09	0.01	0.62	0.62	0.001	−0.84	−0.84	0.94	RPE0	S04
4.15632	44.36920	0.14	0.07	0.09	0.08	−0.003	−0.31	−0.31	0.36	BANN	
4.28660	44.13809	−0.19	−0.05	0.43	0.43	0.001	−0.60	−0.60	0.64	CBR0	S15
4.28747	45.12457	0.32	0.33	0.11	0.10	−0.003	−0.61	−0.42	0.37	TENC	
4.41130	44.76419	0.04	0.28	0.43	0.43	0.000	−0.66	−0.66	0.63	RPA0	S15
4.42164	43.44915	−0.18	−0.18	0.18	0.15	0.000	−2.44	−0.09	0.51	STMR	
4.46692	44.25545	−0.04	0.03	0.07	0.07	−0.004	−0.59	−0.59	0.30	SAUV	
4.53860	45.87707	−0.56	0.49	0.61	0.62	0.000	0.47	0.47	0.92	SAR0	S04
4.67658	45.87909	0.01	0.11	0.08	0.08	−0.003	−0.41	−0.41	0.32	SJDV	
4.71463	46.44943	−0.43	0.19	0.62	0.62	0.001	0.84	0.84	0.94	GRC0	S04
4.76638	43.97591	2.22	−0.54	0.63	0.63	0.001	3.23	3.23	1.03	GMN0	S04
4.81046	43.37597	−0.20	0.29	0.12	0.11	−0.001	−0.98	−0.25	0.30	PALI	
4.86177	43.88137	0.02	0.07	0.07	0.07	−0.003	−0.36	−0.36	0.39	CHRN	
4.95516	47.24282	0.17	0.09	0.61	0.62	0.001	0.04	0.04	0.93	FIX0	S04
5.14972	43.80369	2.71	−0.34	0.62	0.63	0.002	0.98	0.98	0.98	LUB0	S04
5.20090	45.28588	0.14	0.49	0.62	0.62	0.000	0.14	0.14	0.96	VIR0	S04
5.28993	43.37510	−0.41	0.65	0.63	0.63	0.002	0.36	0.36	1.00	RVE0	S04
5.32268	44.89234	−0.04	−0.13	0.43	0.43	0.000	5.85	5.85	0.64	FUR0	S15
5.34203	46.20517	−0.20	0.08	0.61	0.62	0.001	1.25	1.25	0.93	CEY0	S04
5.34265	44.30211	−0.40	0.15	0.61	0.61	0.000	0.68	0.68	0.90	VER0	S04
5.35360	48.48615	−0.36	0.45	0.16	0.11	−0.001	−0.01	−0.76	0.48	BUAN	
5.35379	43.27877	0.33	−0.04	0.11	0.11	0.002	−4.97	−4.20	0.34	MARS	
5.36747	47.79469	−0.04	−0.07	0.62	0.62	0.001	0.12	0.12	0.97	NCH0	S04
5.39846	45.11663	0.15	0.00	0.11	0.09	0.000	0.23	−1.15	0.46	LFAZ	
5.46974	45.75991	−0.09	0.76	0.61	0.61	0.000	−2.21	−2.21	0.90	CRM0	S04
5.48370	43.94096	−0.13	−0.01	0.10	0.08	−0.001	−0.28	−0.29	0.31	RSTL	
5.55184	45.07252	−0.48	0.10	0.21	0.12	−0.002	−0.17	−0.88	0.66	VILR	RGP
5.62465	45.91608	0.08	0.17	0.12	0.08	−0.000	0.38	−1.33	0.33	LEBE	
5.64348	46.64628	−0.03	−0.10	0.62	0.62	0.001	−0.90	−0.90	0.95	PUB0	S04
5.65324	44.95607	−0.38	−0.28	0.16	0.11	−0.001	−0.07	−0.27	0.53	AVR1	
5.71736	43.92416	−0.22	−0.04	0.07	0.06	−0.003	−0.70	−0.70	0.31	MICH	
5.75761	45.88121	0.28	0.01	0.43	0.43	0.000	0.33	0.33	0.63	CUE0	S15
5.76178	45.23522	−0.32	0.02	0.08	0.07	−0.001	0.58	0.58	0.39	STEY	
5.76743	45.09999	−0.38	−0.02	0.43	0.43	0.000	6.39	6.39	0.65	MTC0	S15
5.78698	43.67572	−0.09	0.19	0.08	0.08	−0.003	0.89	0.89	0.60	GINA	
5.79566	46.52858	0.04	0.28	0.07	0.07	−0.004	−0.00	−0.00	0.26	JOUX	
5.88108	45.11072	−0.39	−0.30	0.09	0.09	−0.000	0.13	0.13	0.42	CHAM	
5.88628	46.96544	0.47	0.03	0.61	0.62	0.001	−1.34	−1.34	0.93	CXP0	S04
5.89020	43.16344	0.09	0.72	0.62	0.62	0.001	0.38	0.38	0.94	BAU0	S04
5.90466	43.69322	−0.18	0.32	0.62	0.62	0.001	1.13	1.13	0.94	SJU0	S04
5.90922	45.58128	0.02	−0.17	0.13	0.14	−0.001	−0.25	−1.38	0.47	CBRY	RGP
5.91122	44.68439	−0.32	0.12	0.43	0.43	0.000	0.86	0.86	0.63	CTA0	S15
5.98569	45.64300	0.06	0.17	0.08	0.08	−0.005	−0.07	−0.07	0.33	FCLZ	
6.05166	44.24825	0.06	0.12	0.43	0.43	0.001	0.01	0.01	0.63	PEC0	S15
6.06492	45.52280	−0.05	0.47	0.62	0.62	0.001	0.16	0.16	0.96	CDM0	S04
6.08346	45.08662	−0.15	0.13	0.12	0.09	−0.001	−0.85	−0.25	0.57	ALPE	
6.10204	46.45409	0.53	0.86	0.63	0.64	0.001	−1.74	−1.74	1.05	GIV0	S04
6.10863	45.79444	−0.01	0.45	0.43	0.43	0.000	0.86	0.86	0.63	DTG0	S15
6.12617	47.03998	0.05	0.07	0.53	0.50	0.003	1.62	0.09	1.75	FLGY	
6.20709	45.22545	−0.08	0.11	0.43	0.44	−0.000	2.23	2.23	0.66	CFE0	S15
6.32730	43.98840	−0.34	−0.05	0.62	0.62	0.001	0.47	0.47	0.94	CHA0	S04

Table 1 *(continued)*

Longitude (°E)	Latitude (°N)	V_{east} (mm/year)	V_{north} (mm/year)	Sig V_{east} (mm/year)	Sig V_{north} (mm/year)	Corr.	V_{vert} (mm/year)	Sig V_{vert} (mm/year)	Corr.	SITE	Network
6.35856	45.30414	−0.46	−0.07	0.07	0.08	0.002	1.80	1.80	0.31	CHTL	
6.36669	43.87354	−0.03	0.09	0.23	0.20	0.001	−0.11	0.04	0.55	BLIX	
6.37339	47.04575	0.02	0.18	0.62	0.62	0.002	−2.79	−2.79	0.95	ARC0	S04
6.46553	46.19798	0.16	−0.04	0.43	0.43	0.001	−0.14	−0.14	0.63	PLJ0	S15
6.47896	44.85767	0.56	−0.08	0.11	0.11	−0.000	1.06	−0.71	0.38	PUYA	
6.47897	44.85771	0.10	1.21	0.64	0.64	−0.001	1.31	1.31	0.98	PAV0	S04
6.48765	45.99343	−0.07	0.35	0.93	0.94	0.000	−0.78	−0.78	1.45	AUF0	S04
6.49523	46.83034	0.24	1.05	0.64	0.65	0.003	13.64	13.64	1.12	CTE0	S04
6.51071	46.08442	0.31	0.39	0.25	0.30	−0.001	0.82	−0.67	0.88	MARG	RGP
6.57004	44.73448	−0.03	−0.14	0.39	0.39	0.001	2.12	2.12	0.57	CHP0	S15
6.60101	43.21949	−0.10	0.05	0.10	0.10	−0.000	−0.46	0.09	0.29	TROP	
6.60105	43.21948	−0.04	0.21	0.62	0.62	0.001	−0.29	−0.29	0.93	MPA0	S04
6.62823	45.69149	−0.21	−0.19	0.16	0.10	−0.001	1.40	0.76	0.43	ROSD	
6.62825	45.69158	−0.88	−0.01	0.43	0.43	−0.000	0.99	0.99	0.63	RSL0	S15
6.66187	44.66225	0.09	−0.06	0.20	0.18	−0.000	−0.08	−0.07	0.60	GUIL	
6.71004	44.91036	0.34	−0.29	0.10	0.12	−0.001	1.24	−4.90	0.53	JANU	
6.71009	45.21378	−0.01	−0.38	0.08	0.06	−0.005	1.36	1.36	0.34	MODA	
6.74154	45.22314	0.04	−0.55	0.43	0.43	0.000	2.77	2.77	0.64	AUS0	S15
6.82723	47.91609	0.12	0.29	0.61	0.62	0.001	−1.13	−1.13	0.92	TCH0	S04
6.86584	45.65320	−0.73	−0.54	0.43	0.43	0.000	1.88	1.88	0.63	PSB0	S15
6.94863	47.40972	0.13	0.35	0.62	0.63	0.000	−1.81	−1.81	0.95	FAH0	S04
6.97707	44.26782	−0.11	−0.10	0.16	0.14	−0.001	0.42	0.10	0.43	RABU	
7.03153	47.92301	0.15	0.03	0.12	0.11	−0.000	0.34	−0.53	0.62	MAKS	
7.05410	43.61143	0.13	0.03	0.07	0.07	−0.001	−0.51	−0.51	0.30	SOPH	
7.05767	47.13277	−0.09	1.52	0.63	0.64	0.004	11.29	11.29	1.06	CHS0	S04
7.06108	45.76977	−0.52	−0.47	0.12	0.11	−0.001	1.21	−0.23	0.48	MRGE	RIN
7.06758	46.60839	0.36	1.30	0.63	0.64	0.000	14.46	14.46	1.06	TRE0	S04
7.12188	44.88430	0.76	−0.18	0.94	0.96	−0.000	2.98	2.98	1.59	LAU0	S04
7.13962	45.46794	0.06	−0.45	0.13	0.14	−0.001	0.85	0.20	0.46	AGNE	GAI
7.14287	45.47900	0.32	0.01	0.94	0.96	0.000	4.43	4.43	1.60	NIV0	S04
7.15357	44.20357	−1.17	−0.82	0.62	0.62	0.003	1.33	1.33	0.95	CLB0	S04
7.19671	48.21685	0.28	−0.14	0.16	0.13	−0.001	−0.09	−0.33	0.92	AUBU	
7.26819	47.43835	0.08	0.35	0.12	0.10	−0.001	0.13	−0.44	0.50	LUCE	
7.29998	43.72550	0.22	0.08	0.07	0.08	−0.000	0.10	0.10	0.39	NICE	
7.35130	48.41517	−0.07	−0.04	0.08	0.08	−0.004	−1.71	−1.71	0.62	WLBH	
7.36421	48.87303	−0.33	0.12	0.15	0.14	0.001	0.28	−0.60	0.45	ERCK	
7.37801	47.73329	−0.01	0.18	0.18	0.21	0.000	−0.11	−0.39	0.69	RIXH	
7.40041	43.79280	0.12	0.30	0.63	0.63	0.004	−0.51	−0.51	1.03	CSP0	S04
7.46528	46.87710	0.07	0.42	0.06	0.07	−0.001	0.87	0.87	0.28	ZIMM	IGS
7.66128	45.06337	0.00	0.11	0.13	0.13	0.001	−0.29	−0.05	0.36	TORI	IGS
7.68382	48.62166	0.10	0.15	0.07	0.07	−0.000	−0.29	−0.29	0.39	STJ9	
7.72311	46.32641	−0.07	1.18	0.63	0.63	−0.002	14.76	14.76	1.04	JEI0	S04
7.78873	44.25093	3.24	0.57	0.95	0.96	0.003	−2.10	−2.10	1.58	PRN0	S04
7.99188	45.65842	0.33	0.48	0.96	0.97	−0.004	1.42	1.42	1.86	SGG0	S04
8.08113	44.44599	0.61	−0.13	0.17	0.17	0.002	−0.01	0.04	0.54	PARO	GAI
8.26100	46.31356	−0.26	0.43	0.12	0.12	−0.004	0.93	13.16	0.62	DEVE	GAI
8.68021	46.04234	−0.14	0.17	0.11	0.09	0.000	0.75	−1.27	0.37	CARZ	GAI
8.73259	42.02421	0.64	1.10	0.63	0.63	0.002	−0.14	−0.14	0.96	BSB0	S04
8.76262	41.92746	0.01	0.11	0.08	0.12	0.003	0.02	0.16	0.26	AJAC	
8.92115	44.41939	0.17	0.10	0.07	0.06	0.000	−0.75	−0.75	0.32	GENO	IGS
9.30174	42.64669	−0.18	0.79	0.63	0.64	0.006	1.03	1.03	1.04	MAZ0	S04
9.85026	46.17004	−0.09	0.07	0.28	0.29	−0.002	1.14	−0.29	0.49	SOND	GAI

Note. The last column specifies the network: no entry is RENAG, S04 the Alps survey until 2004, S15 the Alps survey until 2015, IGS the global IGS network, RGP the French permanent reference network from IGN, RIN the Italian permanent network RING from INGV, and GAI stations from the continuous GAIN network (Interreg IIIB project ALPS-GPSQUAKENET).

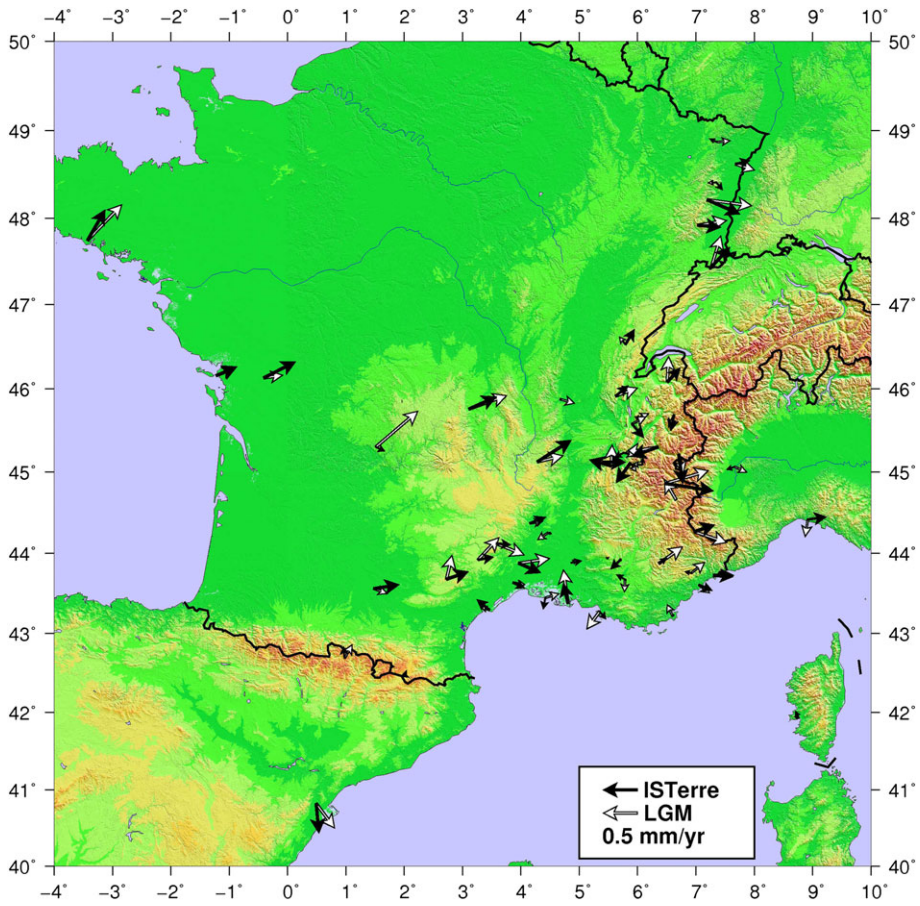

Figure 5. Superposition of the ISTerre and the LGM velocity solutions of 53 common sites using a Helmert transformation to minimize the velocity differences. The largest differences are related to young stations.

4.2. Velocity Profiles Perpendicular to the Arc

Another way to highlight the redundancy between close-by stations is to analyze their velocities on profiles across the mountain belt. In Figure 7 we present a northern and a southern profile, each of them drawn perpendicular to the local orientation of the arc. In the upper graph for each profile, the arc-parallel velocity components of each station are plotted with respect to horizontal distance along the profile. For the faults running parallel to the arc, these arc-parallel velocities represent the strike-slip component. In the lower graph we plot arc-perpendicular velocity components, indicating arc-perpendicular shortening or extension. We fit straight lines through subsets of the velocity data to identify persistent trends over several stations (numerical values in Table 3). The derived trend for the arc-parallel components for both profiles suggests a right-lateral strike slip parallel to the belt, with the highest value of about 0.5 mm/year over a distance of ~130 km for the northern profile. For the arc-perpendicular component, we see three zones with alternating behaviors, showing compression in the foothills/foreland regions (red lines), and extension in the core of the belt (blue line). Once again, the highest values occur along the northern profile with extension rates up to 15 nanostrain/year, and compression rates on the order of 5 nanostrain/year. The extension and compression rates for the southern profiles are 3 nanostrain/year and 1 nanostrain/year, respectively. This difference between the northern and southern part of the Western Alps has been pointed out previously by Nguyen et al. (2016) on the basis of a correlation between the uplift rates and the mean elevation for the northern region that is absent for the southern part. This is also correlated with the lower topography along the southern profile (Figure 7).

The same analysis of the velocity field on the two transects was conducted for the independent LGM solution. The same deformation patterns can be identified: extension framed by compression and right-lateral strike

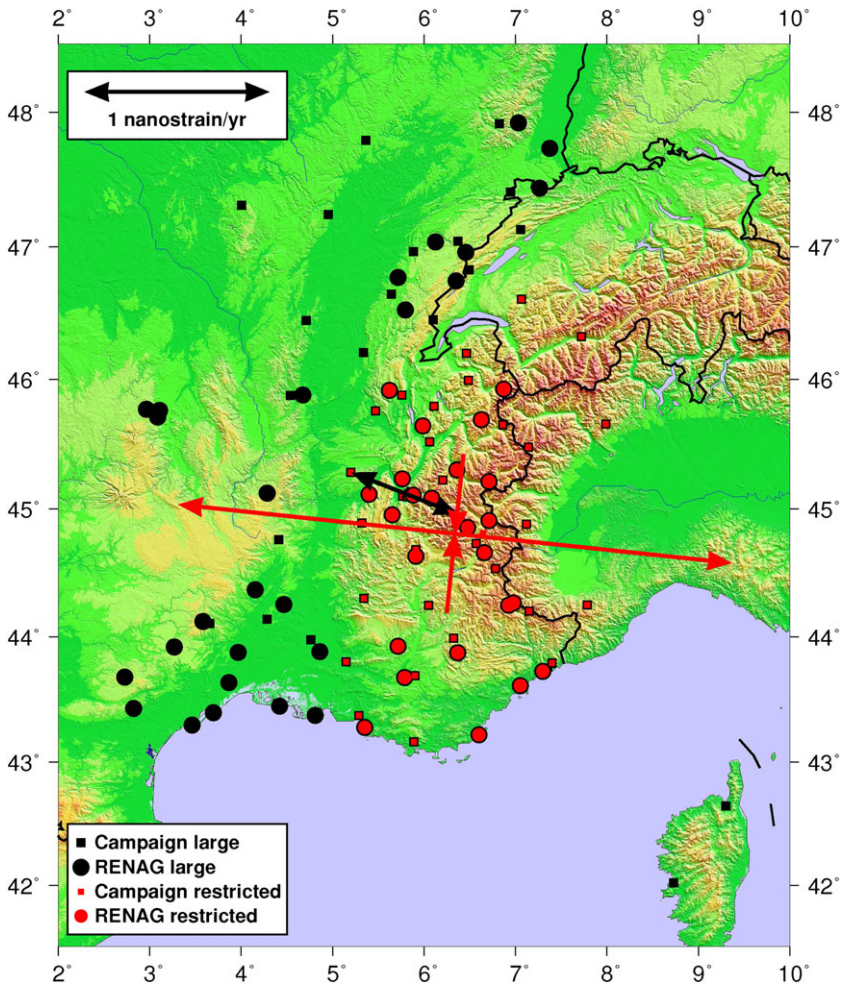

Figure 6. Strain rate tensors calculated over a network with large coverage of the Western Alps (black tensor and black and red station symbols) and with a coverage restricted to the Alpine arc itself (red tensor and red station symbols). The represented tensors are calculated combining the RENAG and the Alps campaign stations (circles and squares, respectively). Numerical values are shown in Table 2.

slip on both profiles. The numerical values (Table 3) are consistent with the ISTerre solution within the error limits. Therefore, we are confident that these features, extension in the core of the belt with compression in the forelands, and noticeable longitudinal right-lateral strike slip across the Western Alps, are well-resolved deformation patterns.

Table 2
Strain Rate Tensors for the Different Network Compositions

Coverage	Strain tensor component	RENAG only	RENAG + campaign stations
Large	Eps1 (nanostrain/year)	0.67 ± 0.17	0.61 ± 0.17
	Eps2 (nanostrain/year)	−0.11 ± 0.11	−0.08 ± 0.11
	Azimuth (° from N)	111.5 ± 7.4	111.5 ± 8.1
Restricted to the Alpine belt	Eps1 (nanostrain/year)	3.15 ± 0.43	3.03 ± 0.43
	Eps2 (nanostrain/year)	−0.94 ± 0.22	−0.87 ± 0.22
	Azimuth (° from N)	95.9 ± 3.3	96.0 ± 3.4

Note. Strain rate tensor components for the different network compositions with large and restricted coverage, for RENAG stations only and for RENAG plus campaign stations. Eps1: most extensional eigenvalue of strain tensor. Eps2: most compressional eigenvalue of strain tensor. Extension is taken positive. Azimuth is the one of Eps1 (extension) in degrees clockwise from north.

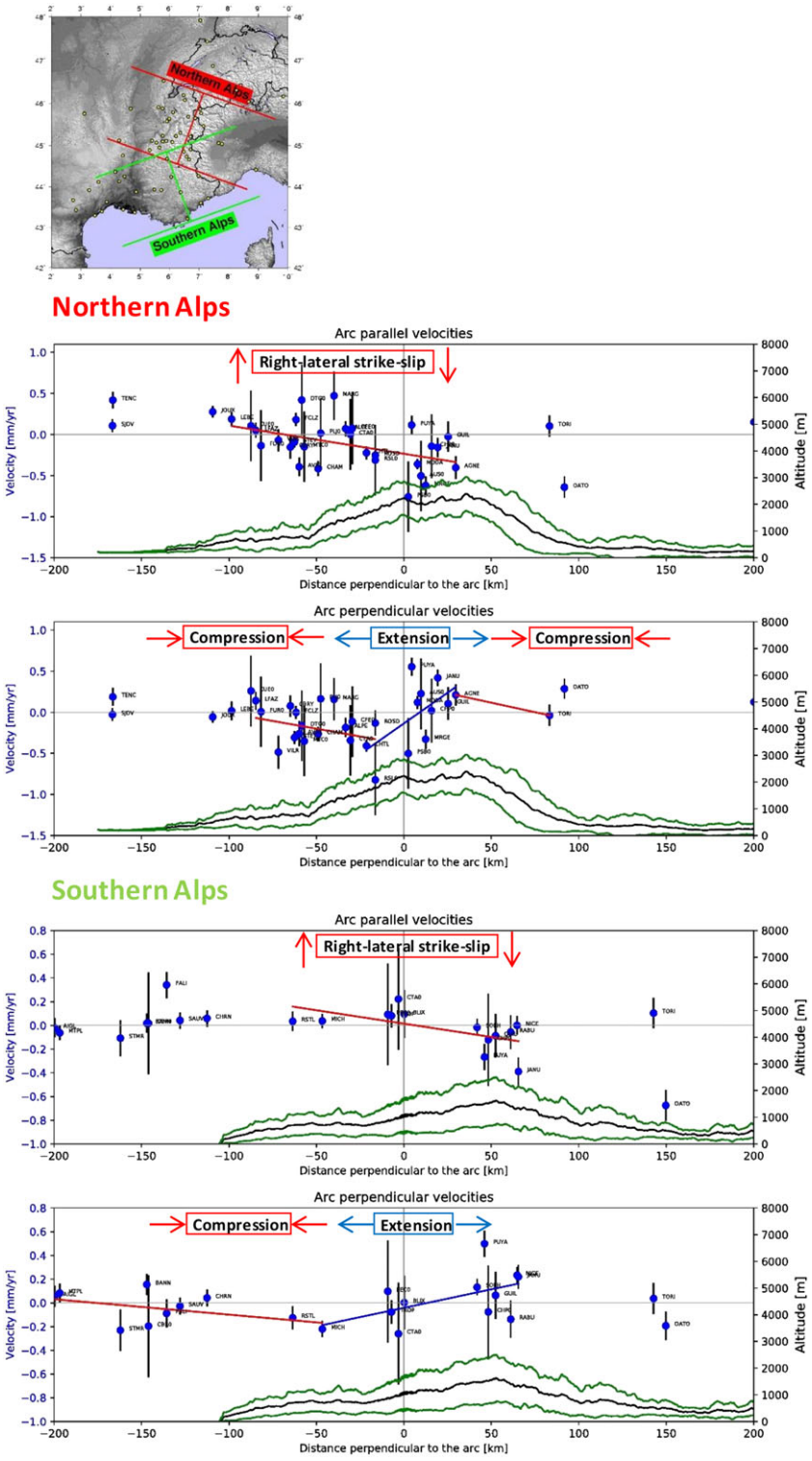

Figure 7. Velocity components for the stations of the ISTerre solution along two arc-perpendicular profiles. The locations of the northern and the southern profile are shown on the map. On the profiles, the *x* axis indicates the distance along the arc-perpendicular profile. Arc-parallel velocity components indicate lateral slip along the arc, and arc-perpendicular velocity components indicate across arc shortening or extension. Straight lines indicate coherent tendencies over subsets of stations. Right lateral strike slip and compression are indicated in red, extension in blue. Numerical values are given in Table 3. The black curves represent the average topography along the profile and the green curves the minimum and maximum values.

Table 3
Comparison of Strain Rate Evaluations on Velocity Profiles

Velocity component	Solution	West (nanostrain/year)	Center (nanostrain/year)	East (nanostrain/year)
North parallel	ISTerre		−3.9 ±1.3 (RL)	
	LGM		−4.6 ±0.8 (RL)	
North perpendicular	ISTerre	−3.8 ±2.8 (SH)	14.9 ±6.1 (EX)	−4.6 (SH)
	LGM	−5.3 ±1.5 (SH)	23.3 ±6.2 (EX)	−2.4 ±2.1 (SH)
South parallel	ISTerre		−2.3 ±0.9 (RL)	
	LGM		−1.3 ±1.1 (RL)	
South perpendicular	ISTerre	−1.3 ±0.9 (SH)	3.1 ±1.5 (EX)	No sites
	LGM	−1.5 ±0.6 (SH)	3.3 ±0.5 (EX)	No sites

Note. Comparison of strain rate evaluations in different parts of the northern and southern velocity profiles from independent geodetic solutions ISTerre and LGM. RL, EX, and SH stand for right-lateral strike slip, extension, and shortening, respectively.

4.3. Geodetic Deformation Map

To further increase the spatial resolution of the Alpine deformation pattern, while still exploiting redundancies in our GPS measurements, we invert the velocity differences on baselines between all station couples across the network to produce a regional strain map. The contributions of these baselines are evaluated in each cell of a regular grid covering the network. This has been done using the STIB software (Strain Tensor from Inversion of Baselines; Masson et al., 2014). The STIB method has three advantages over more classical methods of strain rate calculations using triangles formed by neighboring stations or by the four corner points of regular grid cells on which the station velocities are interpolated: (1) the spatial resolution of the strain field is increased to better than the interstation distance by using all available baselines crossing the grid cell, (2) the influence of a velocity outlier is strongly decreased as it is confined to a much smaller region around the erroneous station compared to strain rate calculations in triangles or interpolated grid cells, and (3) in each STIB grid cell, the strain rate depends not only on the three or four closest velocities but on all velocity estimations on baselines crossing the cell, thereby exploiting redundancy in the velocity field and increasing the signal-to-noise ratio.

Figure 8 shows a map of the geodetically measured strain rates for the Western Alps, determined using the STIB method, and plotted on a regular grid of 0.5° × 0.5° resolution. Only significant strain rate tensors are plotted, according to the resolution factor (higher than 0.5) calculated by STIB (Masson et al., 2014). Compressional strain tensor axes are shown in red and extensional axes in blue. The results obtained along the northern and southern velocity profiles (see above) are confirmed, with compressional strain occurring either side of the range, and extension located in the core of the belt. The strain rate map also shows the maximum amount of deformation (extension and compression) located in the northern part of the Western Alps. The strain rates decrease southward to the Southern Alps and northward to the Swiss Alps. The decrease toward the south is well constrained by the homogeneity and density of our network and is consistent with the reported decrease in uplift rates (Ngyuen et al., 2016; Nocquet et al., 2016). However, the decrease toward the Swiss Alps may be biased by the scarcity of velocities in Switzerland.

5. Discussion

5.1. Confrontation of Geodetic Horizontal Deformation and Seismic Deformation

The distribution of geodetic deformation rates can be compared with a map showing the regional deformation style from the analysis of earthquake focal mechanisms (Delacou et al., 2004; Figure 8). The deformation style is determined from the dip of the compressional *P* and extensional *T* axes of a set of 389 focal mechanisms covering the Western Alps. Extension is characterized by near vertical *P* axes, whereas compression is characterized by near-vertical *T* axes. For each focal mechanism, the most vertical axis is taken into account, assigning negative angles to *T* axis dips and positive angles to *P* axis dips. This parameter thus ranges linearly from −90 (pure extension) over 0 (pure strike slip) to +90 (pure compression) and allows the deformation style to be interpolated across the region. Figure 8 shows the deformation map obtained from focal mechanisms alongside the geodetic strain tensors obtained in our analysis; both data sets are consistent, indicating a

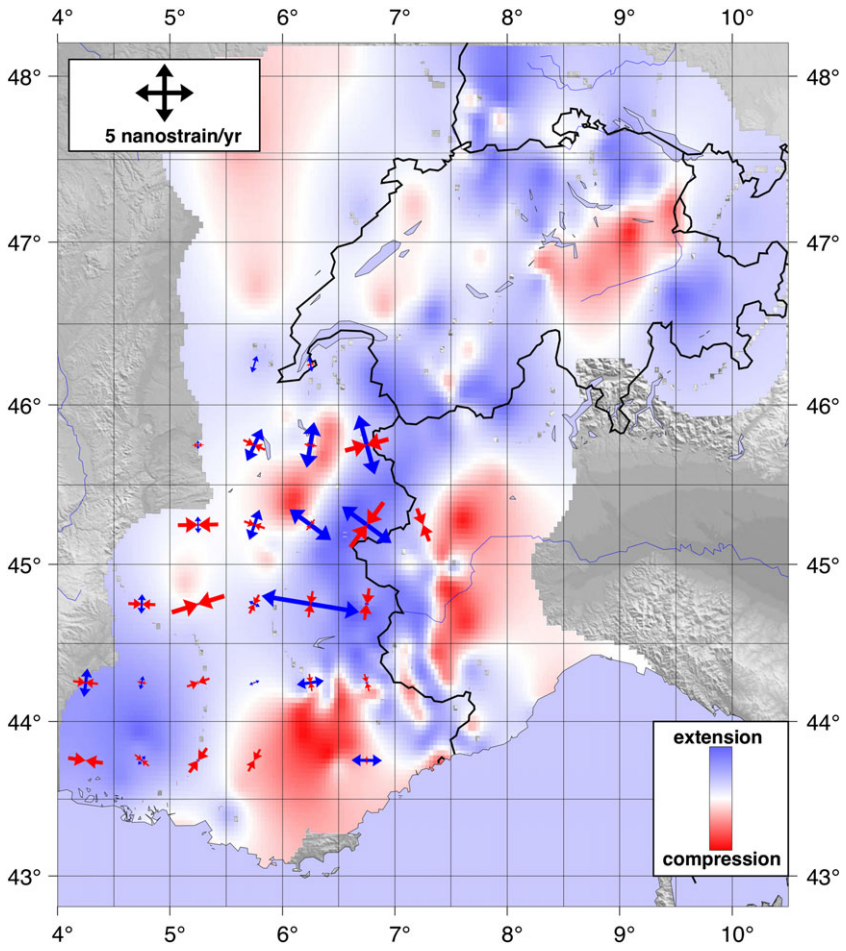

Figure 8. Map of geodetic deformation (arrows), showing the principle axes of GPS strain rate tensors on a regular 0.5 × 0.5° grid. Extension is marked by blue arrows, compression by red arrows. The scale of 5 nanostrain/year corresponds to a deformation rate of 0.5 mm/100 km/year. Background color indicates the patterns of seismic deformation inferred from focal mechanisms by Delacou et al. (2004), with zones of compression in red and zones of extension in blue.

generalized extension in the core of the belt and localized compression along its outer limits. This means that seismicity and horizontal surface deformation are coherent at this level of resolution, which is remarkable in the context of the slow deformation characterizing the Alpine region. While the information of the seismic deformation map of Delacou et al. (2004) is limited just to the mechanism of deformation, our geodetic strain rate map records both the style and amplitude of the deformation, and therefore provides a major new contribution to the characterization of the Western Alps kinematics.

5.2. Confrontations of Geodetic Horizontal Deformation, Geodetic Uplift, and Seismicity

The horizontal deformation field is compared with the vertical station motions from the ISTerre solution (Table 1, color circles on Figure 9, and interpolated with the GMT "blockmean" routine, which calculates block averages using the L2 norm). The highest uplift rates reach values of 2 mm/year in the center of the Northwestern Alps, confirming and refining results presented before by Serpelloni et al. (2013), Nocquet et al. (2016), and Nguyen et al. (2016). The red rectangle roughly delineates the area where extension is dominant. In this zone, the horizontal extension is associated with the highest uplift rates. This implies that the extension in the heart of the mountain belt is not related to gravitational collapse at the end of the orogenic phase (Selverstone, 2005), since it would be associated with subsidence. Similarly, extensional motion across a tectonic plate boundary should be related to subsidence. Possible mechanisms to explain the simultaneous presence of extension and uplift of the Alps have been discussed by Sue, Delacou, Champagnac, Allanic, Tricart et al. (2007), Champagnac et al. (2007), Gardi et al. (2010), Vernant et al. (2013), Nocquet et al. (2016),

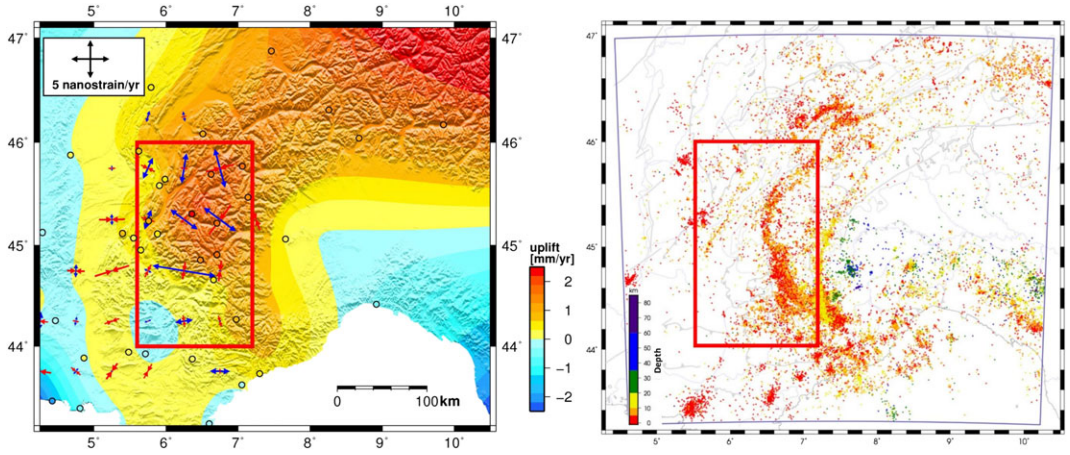

Figure 9. (left) Comparison of the horizontal strain rate field with the map of interpolated vertical displacements (observed station velocities indicated by color circles) and (right) the distribution of 35,000 earthquakes from the French Sismalp network (Potin, 2016). The red rectangle highlights the same geographical zone in the two maps. Color-filled circles on the left plot show the location of GPS stations and their amount of uplift. Color code of the seismicity map on the right indicates the depth of the events.

Chéry et al. (2016), and Mey et al. (2016), and include the cumulative effects of erosional unloading (which also predicts shortening along the edge of the belt), glacial isostatic adjustment combined with a laterally varying rheology of the lower crust and the upper mantle, and uplift due to the presence of a low-viscosity zone in the mantle (Fox et al., 2015; Lippitsch, 2003; Zhao et al., 2015) beneath the area of maximum uplift, thus creating dynamically sustained topography by more buoyant material in the mantle.

Low strain rates and elusive deformation patterns characterize the study area. We thus focus our investigation on the location of maximum extension, maximum uplift, and maximum seismicity (Figure 9) to assess the processes responsible for the observed deformation. Although not yet well constrained, the maximum uplift and the maximum horizontal extension do not appear to be co-located, while the majority of the seismicity is located in the region of maximum horizontal extension. If these observations become clearer with additional time and increase of data, and prove to be significant, the offset north of the region of maximum of uplift may imply that several processes are at work. The maximum uplift could be related to glacial unloading; part of the juxtaposition of extension and compression could be explained by postglacial rebound (short-term) and erosion (long-term), while the enhanced extension in the south, if not fully related to uplift, may result from the relative motion between Western Europe and Apulia. This would also explain the right-lateral shear across the northern part of the Western Alps. However, a dense and unified velocity field at the scale of the Alps is needed to test these hypotheses, while numerical modeling will help to decipher the role of the low-viscosity zone in the mantle, as well as external processes (erosion and deglaciation).

6. Conclusions

Our results support the deformation pattern of the Western Alps previously proposed based on the regional seismicity (Delacou et al., 2004). Combining individual station velocities on belt-perpendicular profiles in the northern and southern parts of the Western Alps, we observe extension in the center of the belt: 15 nanostrain/year in the north decreasing to 3 nanostrain/year in the south. Compression in the forelands decreases from 8 to 1.5 nanostrain/year from north to south. Additionally, the geodetic velocity field indicates right-lateral strike slip of about 0.5 mm/year distributed over a 130-km-wide zone in the northern part of the Alps. The decrease of right-lateral strike slip in the southern part of the Alps, coupled with the absence of relative motions between the extremities of the northern profile (stations SJDV close to Lyon and TORI in Torino), seem to indicate that the pole of the Adriatic microplate is situated close to Torino. For a NS oriented plate boundary between stable Eurasia and the Adriatic in the Western Alps, this pole location predicts pure strike-slip motion at the latitude of Torino, and a decrease of strike-slip motion in favor of extension toward the south.

For the vertical component, our work confirms uplift in the Western Alps, as seen in previous works (Nguyen et al., 2016; Nocquet, 2011; Nocquet et al., 2016; Serpelloni et al., 2013), decreasing from 2 mm/year in the north to 0.3 mm/year in the south. The association of horizontal extension to vertical uplift in the high-topography areas precludes extensional plate tectonics or gravity collapse as they both imply subsidence. While previous works have proposed mechanisms to explain the uplift and extension (e.g., Chéry et al., 2016; Nocquet et al., 2016; Vernant et al., 2013), the increased resolution of our long-term geodetic network suggests that the maximum uplift might be offset with respect to the maximum extension, with the amplitude of horizontal extension being roughly correlated with the seismicity. Therefore, a combination of several processes might be needed to fully understand and explain the present-day deformation of the Western Alps, such as the superposition of postglacial rebound and rotational plate tectonics.

In this work, we have improved the signal-to-noise ratio of long-term GPS measurements in the slowly deforming Western Alps by exploiting the redundancy between (1) cGPS and sGPS networks, (2) independent geodetic solutions, and (3) resulting individual station velocities. Long-term GPS campaign networks have proved to be especially valuable for densifying permanent networks. The 3-D deformation pattern provides new quantitative constraints for geodynamic models of the Western Alps.

Appendix A1

The RENAG team members are listed below.

S. Baize, IRSN, Fontenay-aux-Roses, France

P. Bascou, ISTerre, Université Savoie Mont Blanc, Chambéry, France

S. Baudin, Géosciences Montpellier, Université Montpellier, France

O. Bock, LAREG/IGN, Paris, France

P. Briole, ENS Paris, France

J. Cali, ESGT, Le Mans, France

J.-P. Cardagliaguet, CNES, Toulouse, France

C. Champollion, Géosciences Montpellier, Université Montpellier, France

O. Charade, DT INSU, Meudon, France

J. Chéry, Géosciences Montpellier, Université Montpellier, France

N. Cotte, ISTerre, Université Grenoble Alpes, France

O. Dauteuil, Géoscience Rennes, Université Rennes, France

E. Doerflinger, Géosciences Montpellier, Université Montpellier, France

T. Duquesnoy, SGN/IGN, St. Mandé, France

S. Durand, ESGT, Le Mans, France

R. Fages, SGN/IGN, St. Mandé, France

G. Ferhat, EOST, Université Strasbourg, France

M. Flouzat, CEA-LDG, Arpajon, France

B. Garayt, SGN/IGN, St. Mandé, France

M. Gay, GIPSA-lab, Université Grenoble Alpes, France

M. Gravelle, LIENSs, Université La Rochelle, France

M. Guichard, LIENSs, Université La Rochelle, France

J. Hinderer, EOST, Université Strasbourg, France

F. Jouanne, ISTerre, Université Savoie Mont Blanc, Chambéry, France

C. Lallemand, CEA-LDG, Arpajon, France

F. Masson, EOST, Université Strasbourg, France

E.-R. Mathis, SGN/IGN, St. Mandé, France

S. Mazzotti, Géosciences Montpellier, Université Montpellier, France

J.-L. Menut, Géoazur, Université Nice, Sophia-Antipolis, France

F. Moreau, Géosciences Rennes, Université Rennes, France

L. Morel, ESGT, Le Mans, France

J. Nicolas, ESGT, Le Mans, France

J.-M. Nocquet, Géoazur, Université Nice, Sophia-Antipolis, France

L. Ott, GIPSA-lab, Université Grenoble Alpes, France

F. Perosanz, GET, Université Toulouse, France

T. Person, SGN/IGN, St. Mandé, France

E. Poirier, LIENSs, Université La Rochelle, France

A. Rigo, ENS Paris, France

L. Rolland, Géoazur, Université Nice, Sophia Antipolis, France

A. Santamaria-Gomez, GET, Université Toulouse, France

S. Saur, SGN/IGN, St. Mandé, France

O. Scotti, IRSN, Fontenay-aux-Roses, France

A. Socquet, ISTerre, Université Grenoble Alpes, France

P. Ulrich, EOST, Université Strasbourg, France

J. Van Baelen, LaMP, Clermont-Ferrand, France

M. Vergnolle, Géoazur, Université Nice, Sophia Antipolis, France

M. Vidal, Géoazur, Université Nice, Sophia Antipolis, France

C. Vigny, ENS Paris, France

T. Villemin, EDYTEM, Université Savoie-Mont Blanc, Chambéry, France

G. Wöppelmann, LIENSs, Université La Rochelle, France

Acknowledgments

The GPS data used in this study are publicly available data from the RESIF-RENAG network (http://renag.resif.fr), from the RGP network managed by Institut National de l'Information Géographique et Forestière (IGN; http://rgp.ign.fr) also contributing to RESIF, from the cGPS network of the Interreg-B project ALPS-GPSQUAKENET, from the RING network of INGV (http://ring.gm.ingv.it), and from the Alps campaigns available at https://gpscope.dt.insu.cnrs.fr/spip/spip.php?article123. RESIF is a national Research Infrastructure, recognized as such by the French Ministry of higher education and research. RESIF is managed by the RESIF Consortium, composed of 18 research institutions and universities in France. RESIF is supported by a public grant provided by the French National Research Agency (ANR) as part of the "Investissements d'Avenir" program (reference ANR-11-EQPX-0040) and the French Ministry of Environment, Energy, and Sea. This work has also been supported by a grant from LabEx OSUG@2020 (Investissements d'avenir—ANR10LABX56). The methods used in this manuscript are being developed in the framework of the implementation phase (IP) of the European Plate Observing System (EPOS). The EPOS-IP project has received funding from the European Union's Horizon 2020 research and innovation program under grant agreement 676564. We are very grateful to all of the institutes and organizations running permanent GPS stations over decadal time spans, and to the participants of the Alps campaigns in 1993, 1998, 2004, and 2015. We are glad to acknowledge here also the investment in the maintenance of the networks of our former colleagues Jean-Paul Glot, Philippe Collard, Claude Pambrun, and Pascal Tiphaneau. We thank Bertrand Potin for sharing his map of precise relocation of earthquakes in the Alps. Finally, many thanks to Pietro Sternai for the fruitful discussions on geodetic measurements of the Alpine deformation and to James Hollingsworth for the final thorough English language editing.

References

Anderson, H., & Jackson, J. (1987). Active tectonics of the Adriatic region. *Geophysical Journal of the Royal Astronomical Society*, *91*(3), 937–983. https://doi.org/10.1111/j.1365-246X.1987.tb01675.x

Barletta, V. R., Ferrari, C., Diolaiuti, G., Carnielli, T., Sabadini, R., & Smiraglia, C. (2006). Glacier shrinkage and modeled uplift of the Alps. *Geophysical Research Letters*, *33*, L14307. https://doi.org/10.1029/2006GL026490

Battaglia, M., Murray, M. H., Serpelloni, E., & Bürgmann, R. (2004). The Adriatic region: An independent microplate within the Africa-Eurasia collision zone. *Geophysical Research Letters*, *31*, L09605. https://doi.org/10.1029/2004GL019723

Calais, E., Nocquet, J.-M., Jouanne, F., & Tardy, M. (2002). Current strain regime in the western Alps from continuous global positioning system measurements, 1996–2001. *Geology*, *30*(7), 651–654. https://doi.org/10.1130/0091-7613(2002)030<0651:CSRITW>2.0.CO;2

Calais, E., & Stein, S. (2009). Time-variable deformation in the New Madrid seismic zone. *Science*, *323*(5920), 1442–1442.

Champagnac, J. D., Molnar, P., Anderson, R. S., Sue, C., & Delacou, B. (2007). Quaternary erosion-induced isostatic rebound in the western Alps. *Geology*, *35*(3), 195. https://doi.org/10.1130/G23053A.1

Chéry, J., Genti, M., & Vernant, P. (2016). Ice cap melting and low-viscosity crustal root explain the narrow geodetic uplift of the western Alps. *Geophysical Research Letters*, *43*, 3193–3200. https://doi.org/10.1002/2016GL067821

D'Agostino, N., Avallone, A., Cheloni, D., D'Anastasio, E., Mantenuto, S., & Selvaggi, G. (2008). Active tectonics of the Adriatic region from GPS and earthquake slip vectors. *Journal of Geophysical Research*, *113*, B12413. https://doi.org/10.1029/2008JB005860

Delacou, B., Sue, C., Champagnac, J.-D., & Burkhard, M. (2004). Present-day geodynamics in the bend of the western and central Alps as constrained by earthquake analysis. *Geophysical Journal International*, *158*(2), 753–774. https://doi.org/10.1111/j.1365-246X.2004.02320.x

Fox, M., Herman, F., Kissling, E., & Willett, S. D. (2015). Rapid exhumation in the western Alps driven by slab detachment and glacial erosion. *Geology*, *43*(5), 379–382. https://doi.org/10.1130/G36411.1

Gardi, A., Baize, S., & Scotti, O. (2010). Present-day vertical isostatic readjustment of the western Alps revealed by numerical modelling and geodetic and seismotectonic data. *Geological Society, London, Special Publications*, *332*(1), 115–128. https://doi.org/10.1144/SP332.8

Héroux, P., & Kouba, J. (2001). GPS precise point positioning using IGS orbit products. *Physical Chemical Earth*, *26*(6–8), 573–578. https://doi.org/10.1016/S1464-1895(01)00103-X

Herring, T. A., King, R. W., Floyd, M. A., & McClusky, S. C. (2015). *Introduction to GAMIT/GLOBK, Release 10.6*. Cambridge: Massachusetts Institute of Technology.

Lippitsch, R. (2003). Upper mantle structure beneath the alpine orogen from high-resolution teleseismic tomography. *Journal of Geophysical Research*, *108*(B8), 2376. https://doi.org/10.1029/2002JB002016

Masson, F., Lehujeur, M., Ziegler, Y., & Doubre, C. (2014). Strain rate tensor in Iran from a new GPS velocity field. *Geophysical Journal International*, *197*(1), 10–21.

Mey, J., Scherler, D., Wickert, A. D., Egholm, D. L., Tesauro, M., Schildgen, T. F., & Strecker, M. R. (2016). Glacial isostatic uplift of the European Alps. *Nature Communications*, *7*, 1–9. https://doi.org/10.1038/ncomms13382

Nguyen, H. N., Vernant, P., Mazzotti, S., Khazaradze, G., & Asensio, E. (2016). 3D GPS velocity field and its implications on the present-day postorogenic deformation of the western Alps and Pyrenees. *Solid Earth Discussions*, *7*(5), 1349. https://doi.org/10.5194/se -2016-78

Nocquet, J.-M. (2011). Apport de la Géodésie Spatiale à la Connaissance de la Géodynamique en Europe et en Méditerranée Habilitation à diriger des recherches, Université Nice Sophia Antipolis.

Nocquet, J.-M. (2012). Present-day kinematics of the Mediterranean: A comprehensive overview of GPS results. *Tectonophysics*, *579*, 220–242. https://doi.org/10.1016/j.tecto.2012.03.037

Nocquet, J.-M., & Calais, E. (2004). Geodetic measurements of crustal deformation in the western Mediterranean and Europe. *Pure and Applied Geophysics*, *161*(3), 661–681. https://doi.org/10.1007/s00024-003-2468-z

Nocquet, J. M., Sue, C., Walpersdorf, A., Tran, T., Lenôtre, N., Vernant, P., et al. (2016). Present-day uplift of the western Alps. *Scientific Reports*, *6*(1), 28404. https://doi.org/10.1038/srep28404

Nocquet, J.-M., Willis, P., & Garcia, S. (2006). Plate kinematics of Nubia–Somalia using a combined DORIS and GPS solution. *Journal of Geodesy*, *80*(8-11), 591–607. https://doi.org/10.1007/s00190-006-0078-0

Potin, B. (2016). Les Alpes occidentales: tomographie, localisation de séismes et topographie du Moho, (PhD thesis). University Grenoble Alpes.

RESIF (2017). RESIF-RENAG French national Geodetic Network. RESIF - Réseau Sismologique et géodésique Français. https://doi.org/10.15778/resif.rg

Selverstone, J. (2005). Are the Alps collapsing? *Annual Review of Earth and Planetary Sciences*, *33*(1), 113–132. https://doi.org/10.1146/annurev.earth.33.092203.122535

Serpelloni, E., Anzidei, M., Baldi, P., Casula, G., & Galvani, A. (2005). Crustal velocity and strain-rate fields in Italy and surrounding regions: New results from the analysis of permanent and non-permanent GPS networks. *Geophysical Journal International*, *161*(3), 861–880. https://doi.org/10.1111/j.1365-246X.2005.02618.x

Serpelloni, E., Faccenna, C., Spada, G., Dong, D., & Williams, S. D. P. (2013). Vertical GPS ground motion rates in the Euro-Mediterranean region: New evidence of velocity gradients at different spatial scales along the Nubia–Eurasia plate boundary. *Journal of Geophysical Research: Solid Earth*, *118*, 6003–6024. https://doi.org/10.1002/2013JB010102

Serpelloni, E., Vannucci, G., Pondrelli, S., Argnani, A., Casula, G., Anzidei, M., et al. (2007). Kinematics of the Western Africa-Eurasia Plate Boundary From Focal Mechanisms and GPS Data. *Geophysical Journal International*, *169*, 1180–1200. https://doi.org/10.1111/j.1365-246X.2007.03367.x

Stocchi, P., Spada, G., & Cianetti, S. (2005). Isostatic rebound following the alpine deglaciation: Impact on the sea level variations and vertical movements in the Mediterranean region. *Geophysical Journal International*, *162*(1), 137–147. https://doi.org/10.1111/j.1365-246X.2005.02653.x

Sue, C., Delacou, B., Champagnac, J. D., Allanic, C., & Burkhard, M. (2007). Aseismic deformation in the Alps: GPS vs. seismic strain quantification. *Terra Nova*, *19*(3), 182–188. https://doi.org/10.1111/j.1365-3121.2007.00732.x

Sue, C., Delacou, B., Champagnac, J. D., Allanic, C., Tricart, P., & Burkhard, M. (2007). Extensional neotectonics around the bend of the western/central Alps: An overview. *International Journal of Earth Sciences*, *96*(6), 1101–1129. https://doi.org/10.1007/s00531-007-0181-3

Sue, C., Martinod, J., Tricart, P., Thouvenot, F., Gamond, J. F., Frechet, J., et al. (2000). Active deformation in the inner western Alps inferred from comparison between 1972-classical and 1996-GPS geodetic surveys. *Tectonophysics*, *320*(1), 17–29. https://doi.org/10.1016/S0040-1951(00)00024-X

Sue, C., Thouvenot, F., Fréchet, J., & Tricart, P. (1999). Widespread extension in the core of the western Alps revealed by earthquake analysis. *Journal of Geophysical Research*, *104*, 611–622.

Vernant, P., Hivert, F., Chery, J., Steer, P., Cattin, R., & Rigo, A. (2013). Erosion-induced isostatic rebound triggers extension in low convergent mountain ranges. *Geology*, *41*(4), 467–470. https://doi.org/10.1130/G33942.1

Vigny, C., Chéry, J., Duquesnoy, T., Jouanne, F., Ammann, J., Andizei, M., et al. (2002). GPS network monitors the western Alps' deformation over a five-year period: 1993–1998. *Journal of Geodesy*, *76*(2), 63–76. https://doi.org/10.1007/s00190-001-0231-8

Walpersdorf, A., Sue, C., Baize, S., Cotte, N., Bascou, P., Beauval, C., et al. (2015). Coherence between geodetic and seismic deformation in a context of slow tectonic activity (SW Alps, France). *Journal of Geodynamics*, *85*, 58–65. https://doi.org/10.1016/j.jog.2015.02.001

Zhao, L., Paul, A., Guillot, S., Solarino, S., Malusà, M. G., Zheng, T., et al. (2015). First seismic evidence for continental subduction beneath the western Alps. *Geology*, *43*(9), 815–818. https://doi.org/10.1130/G36833.1

Zumberge, J. F., Heflin, M. B., Jefferson, D. C., Watkins, M. M., & Webb, F. H. (1997). Precise point positioning for the efficient and robust analysis of GPS data from large networks. *Journal of Geophysical Research*, *102*(B3), 5005–5017. https://doi.org/10.1029/96JB03860